The structured core domain of αB-crystallin can prevent amyloid fibrillation and associated toxicity

Georg K. A. Hochberg[a,1], Heath Ecroyd[b,c,1], Cong Liu[d,e,f,2], Dezerae Cox[b,c], Duilio Cascio[d,e,f], Michael R. Sawaya[d,e,f], Miranda P. Collier[a], James Stroud[d,e,f], John A. Carver[g], Andrew J. Baldwin[a], Carol V. Robinson[a], David S. Eisenberg[d,e], Justin L. P. Benesch[a,3], and Arthur Laganowsky[a,d,e,f,3]

[a]Physical and Theoretical Chemistry Laboratory, Department of Chemistry, University of Oxford, Oxford OX1 3QZ, United Kingdom; [b]Illawarra Health and Medical Research Institute and [c]School of Biological Sciences, University of Wollongong, Wollongong, NSW 2522, Australia; [d]Howard Hughes Medical Institute, [e]University of California, Los Angeles–Department of Energy Institute for Genomics and Proteomics, and [f]Department of Chemistry and Biochemistry, University of California, Los Angeles, CA 90095; [g]Research School of Chemistry, The Australian National University, Canberra, ACT 0200, Australia

Edited by Gregory A. Petsko, Weill Cornell Medical College, New York, NY, and approved March 11, 2014 (received for review December 5, 2013)

Mammalian small heat-shock proteins (sHSPs) are molecular chaperones that form polydisperse and dynamic complexes with target proteins, serving as a first line of defense in preventing their aggregation into either amorphous deposits or amyloid fibrils. Their apparently broad target specificity makes sHSPs attractive for investigating ways to tackle disorders of protein aggregation. The two most abundant sHSPs in human tissue are αB-crystallin (ABC) and HSP27; here we present high-resolution structures of their core domains (cABC, cHSP27), each in complex with a segment of their respective C-terminal regions. We find that both truncated proteins dimerize, and although this interface is labile in the case of cABC, in cHSP27 the dimer can be cross-linked by an intermonomer disulfide linkage. Using cHSP27 as a template, we have designed an equivalently locked cABC to enable us to investigate the functional role played by oligomerization, disordered N and C termini, subunit exchange, and variable dimer interfaces in ABC. We have assayed the ability of the different forms of ABC to prevent protein aggregation in vitro. Remarkably, we find that cABC has chaperone activity comparable to that of the full-length protein, even when monomer dissociation is restricted through disulfide linkage. Furthermore, cABC is a potent inhibitor of amyloid fibril formation and, by slowing the rate of its aggregation, effectively reduces the toxicity of amyloid-β peptide to cells. Overall we present a small chaperone unit together with its atomic coordinates that potentially enables the rational design of more effective chaperones and amyloid inhibitors.

X-ray crystallography | ion mobility mass spectrometry | nuclear magnetic resonance spectroscopy

The proteome is inherently metastable (1, 2), and therefore the cell is required to maintain protein homeostasis (or "proteostasis") actively through the balancing of a multitude of biochemical pathways (3). The breakdown of this steady state can lead to a variety of diseases, many of which are characterized by the aggregation and deposition of misfolded proteins (4). Molecular chaperones, proteins that act to prevent improper polypeptide associations, are crucial components of the cellular proteostasis machinery (5, 6). They include the small heat-shock proteins (sHSPs), which are found in organisms across all branches of the tree of life and play an important role in preventing protein misfolding and aggregation (7, 8). In general the sHSPs are capable of intercepting destabilized targets (9) and either holding them in a refolding-competent state, preventing them from aggregating into unrecoverable deposits, or directing them toward degradation (10). αB-crystallin (ABC) is an abundant mammalian sHSP, the expression of which is constitutive in most human tissues and upregulated in a variety of pathological disorders (11). The chaperone activity of ABC has been established for more than two decades (12), and it is associated with amyloid fibril deposits in vivo that are characteristic of protein-misfolding diseases including Alzheimer's and Parkinson's diseases (13–15).

Proteins enter the amyloid cascade from their native state and form insoluble fibrils via various intermediates, including oligomeric forms (16, 17). Both amyloid fibrils and oligomers are harmful to cells; however, the latter appear to be more toxic (18). ABC has been shown to mitigate amyloid toxicity to cells in culture (19), to interact directly with amyloid oligomers in vitro (20), and to prevent the fibrillation of a variety of targets (21–25). Additionally ABC has been shown to bind to mature amyloid-β peptide ($A\beta_{1-42}$) (22, 24), α-synuclein (23, 25), and apolipoprotein C-II (apoC-II) fibrils (26), apparently coating them and preventing their elongation (21). An understanding of how ABC carries out these activities has been hindered by the structural and dynamical complexities of this chaperone. ABC, as is typical for most metazoan sHSPs, consists of a dimeric building block that assembles via terminal interactions into a polydisperse ensemble (8). In ABC, these oligomers range from ∼10–50 subunits and readily interconvert via the exchange of monomers (27) in a process that facilitates the formation of

Significance

We find that the core domain of the human molecular chaperone αB-crystallin can function effectively in preventing protein aggregation and amyloid toxicity. The core domain represents only half the total sequence of the protein, but it is one of the most potent known inhibitors of the aggregation of amyloid-β, a process implicated in Alzheimer's disease. We have determined high-resolution structures of this core domain and investigated its biophysical properties in solution. We find that the excised domain efficiently prevents amyloid aggregation and thereby reduces the toxicity of the resulting aggregates to cells. The structures of these domains that we present should represent useful scaffolds for the design of novel amyloid inhibitors.

Author contributions: G.K.A.H., J.A.C., C.V.R., D.S.E., J.L.P.B., and A.L. designed research; G.K.A.H., H.E., C.L., D. Cox, D. Cascio, M.R.S., M.P.C., J.S., A.J.B., and A.L. performed research; G.K.A.H., H.E., C.L., D. Cox, D. Cascio, M.R.S., A.J.B., J.L.P.B., and A.L. analyzed data; and G.K.A.H., H.E., J.A.C., C.V.R., D.S.E., J.L.P.B., and A.L. wrote the paper.

The authors declare no conflict of interest.

This article is a PNAS Direct Submission.

Data deposition: Crystallography, atomic coordinates, and structure factors reported in this paper have been deposited in the Research Collaboratory for Structural Bioinformatics Protein Data Bank (RCSB PDB) database, http://www.rcsb.org (RCSB PDB IDs 4M5S, 4M5T, and 4MJH).

[1]G.K.A.H. and H.E. contributed equally to this work.

[2]Present address: The Interdisciplinary Research Center on Biology and Chemistry, Shanghai Institute of Organic Chemistry, Chinese Academy of Sciences, Shanghai 200032, China.

[3]To whom correspondence may be addressed. E-mail: justin.benesch@chem.ox.ac.uk or art.laganowsky@chem.ox.ac.uk.

This article contains supporting information online at www.pnas.org/lookup/suppl/doi:10.1073/pnas.1322673111/-/DCSupplemental.

hetero-oligomers between different sHSPs (28). Although several new models for ABC oligomers have been developed recently, a consensus as to their quaternary structure remains to be reached (8, 29).

The sequence of ABC can be divided into an Ig-like α-crystallin domain (ACD) that mediates dimerization and is flanked by N- and C-terminal regions that are poorly conserved and variable in length among sHSPs (7, 8). Various regions of the ABC sequence have been implicated as potential binding sites, but there is little consensus (30–34). Moreover, it even remains unclear whether the polydisperse oligomeric ensemble of ABC, the oligomeric dissociation that mediates subunit exchange, or remodeling of the dimer interface is responsible for chaperone function (8). Models have been proposed wherein suboligomeric forms, which are in equilibrium with the assembled state, are the active chaperoning unit. This idea is based on the observation that solution conditions that accelerate subunit exchange also lead to increased chaperone activity (35). Conversely, other studies have demonstrated that ABC still can function as a chaperone despite being cross-linked as an oligomer (36) and that mutations that slow its subunit exchange kinetics do not necessarily diminish its activity as a chaperone in vitro (37).

These apparent conflicts likely stem from the intrinsic heterogeneity of ABC and the difficulty in assessing the interplay between its structural and dynamical aspects (8, 29). Here we have gained insight into the chaperone activity of ABC and the prevention of protein aggregation in general by establishing a minimal but chaperone-active unit of ABC that is suitable for structural studies. We drew inspiration from recent structures of the ACD that have revealed the ABC dimer interface to be composed of paired β6+7 strands (38–41). Interestingly, their antiparallel interaction has been crystallized in two different registers, termed "AP_I" and "AP_{II}" (41), with a third, "AP_{III}," having been found for the related HSP20 (38). The three registration states have different amounts of buried surface area in the dimer interface, resulting from monomers progressively being shifted outward relative to one another in AP_{II} and AP_{III} compared to AP_I. We have engineered a construct comprising exclusively the core domain of ABC (cABC) which allowed us to test the relationship between oligomeric state, subunit exchange, registration state, and chaperone function of ABC.

Our experimental strategy combines X-ray crystallography with native MS and NMR spectroscopy (hereafter, NMR) to examine the structure of cABC. Using a different approach to crystallize the protein, we show that cABC can populate three different registers and that the AP_{II} form is predominant in solution. Through comparison with a structure of the HSP27 core domain (which we also present here), we have engineered a cysteine mutant of cABC ($cABC_{E117C}$) that can be locked into a dimeric state in the AP_{II} registration state. This protein therefore is unable to exchange monomers under oxidizing conditions. We show that both cABC and $cABC_{E117C}$ can strongly inhibit amorphous aggregation, amyloidogenesis, and amyloid toxicity as effectively as the wild-type protein. Together our data demonstrate that the core domain of ABC is responsible for its potent molecular chaperone function, which is retained regardless of stoichiometry or registration state of the dimer.

Results

An Alternative Strategy to Crystallize Mammalian sHSPs. In a novel approach to crystallize mammalian ACDs, we designed a system composed of a core unit of ABC (residues 68–153, cABC) and a peptide mimicking its C-terminal region (residues 156–164, ERTIPITRE) to avoid the runaway domain swapping that resulted in a polymer-like crystal array in our previous study (41). Cocrystallization of cABC and the peptide produced crystals that led to structure determination at 1.35 Å (Table S1). The structure of cABC reveals a crystal packing of tetrameric units, assembled essentially as a dimer of dimers (Fig. 1*A*). One peptide is bound to each cABC monomer in an orientation antiparallel to the β8 strand (Fig. 1*B*), the inverse of that in our previous structure of ABC (41). This bidirectionality is enabled by the palindromic nature of the peptide (42) and is consistent with the binding observed in NMR experiments (43). The two monomers form a dimer interface in which they are slightly bent relative to each other (Fig. 1*A*), reminiscent of a structure of ABC obtained by means of solid-state NMR (40). However, the angle between monomers is larger in our structure, reflecting a flatter interface, and we also observe no intrinsic twist of the monomers (Fig. S1*A*). Notably, we find that the dimer is in the AP_{III} register, a state previously observed only in the structure of HSP20 (38). A comparison of the registers for ABC reveals the AP_{III} structure to have 685.1 $Å^2$ of buried surface area, compared with 694.1 in AP_{II} [Protein Data Bank (PDB) ID code: 2WJ7] and 820.7 $Å^2$ in AP_I (PDB ID code: 3LIG). Together with structures of truncated ABC constructs in the AP_I (41) and AP_{II}

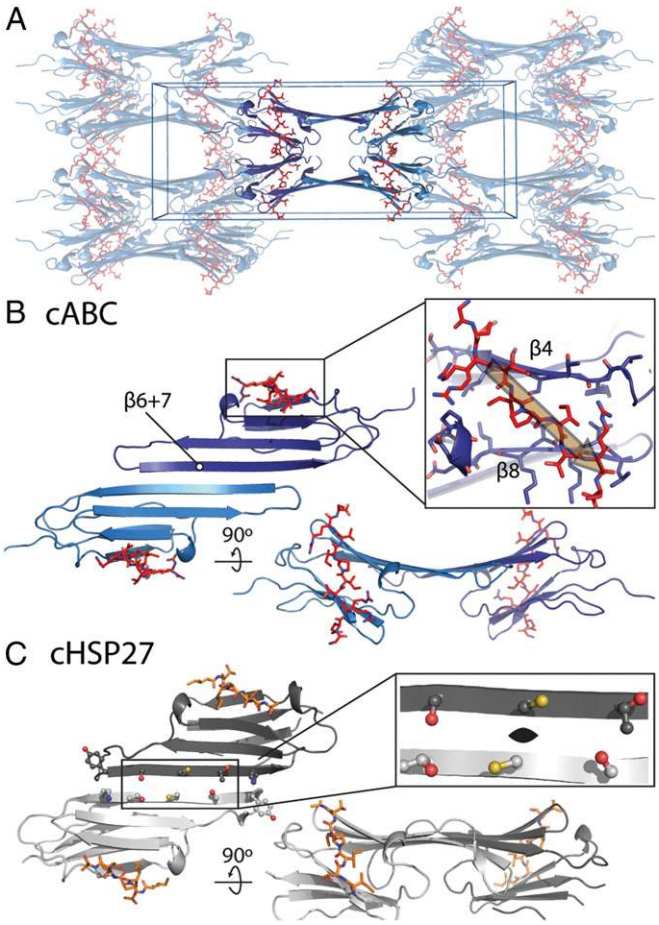

Fig. 1. Crystal structures of cABC and cHSP27. (*A*) cABC crystallizes as a dimer of dimers, with one C-terminal peptide of sequence ERTIPITRE (red) bound to each monomer. (*B*) Two Ig-like cABC monomers assemble into a dimer through pairwise and antiparallel interactions between extended β6+7 strands. In this structure the dimer is found in the AP_{III} register. (*Inset*) The palindromic C-terminal peptide binds to a hydrophobic groove between the β4 and β8 strands, in an antiparallel direction to the β8 strand. The N-to-C direction is illustrated by the yellow arrow. (*C*) The crystal structure of cHSP27 reveals a dimer similar to cABC, rich in β-sheet structure and with C-terminal peptides bound. (*Inset*) cHSP27, however, is in the AP_{II} register, with C137 (thiol colored in yellow) located about a twofold axis at the dimer interface. C137 is reduced in the structure because of the presence of reductant during crystallization but can be oxidized readily (Fig. 4).

states (38–40), this structure in the AP_{III} state shows that ABC can populate multiple dimer interface registers that differ in their buried surface area.

The Core Domain Dimer of HSP27 Has Cysteines Located About a Twofold Axis. To interrogate the potential role of these different registers, we drew inspiration from HSP27, a related human sHSP that has a cysteine residue (C137) located within the β6+7 strand that can be oxidized readily (44). By using our cocrystallization strategy, we succeeded in determining the structure for the HSP27 ACD (residues 86–169, cHSP27) in complex with its C-terminal peptide (residues 179–185, ITIPVTF) (Table S1). We find that cHSP27 forms a canonical dimer in an AP_{II} register and with the C-terminal peptide bound in an antiparallel orientation relative to the β8 strand (Fig. 1*C*). Our structure superimposes well with a previous one in which monomers assembled into a noncanonical hexamer within the crystal lattice (backbone rmsd = 0.45 $Å^2$ comparing monomers; Fig. S1*B*), and the registration state is consistent with small-angle X-ray scattering data (45). The structures are slightly different around the loop between the β5 and β6+7 strands, which contained several point mutations in the previous structure and was disordered. We find this region to be ordered in an extended conformation along the β6+7 sheet of the dimer interface. This difference can be explained by our construct including additional N-terminal residues, allowing the formation of a β2 strand consistent with structures obtained for other metazoan ACDs (Fig. S1*C*).

Differences in the primary sequences of cABC and cHSP27 are distributed over the entire domain, with slightly more disparity observed in flexible loops between successive β-strands (Fig. 2*A*). Although the monomeric fold is nearly identical in the two proteins (Fig. 2*B*), in cHSP27 the β-sandwich is splayed outward by ~2.5 Å. This conformation can be attributed to the combined effect of several substitutions (Fig. S1*E*). The most striking difference, however, is found for residues located next to C137 on the β6+7 strand in HSP27. In cABC there is a charge network of two histidines (H101 and H119) and two glutamates (E99 and E117) that implies pH sensitivity (Fig. 2*C*) (39, 40). In cHSP27, these histidines are replaced by threonines, and E117 is replaced by C137, resulting in a disruption of the charge network (Fig. 2*C*). Moreover, our structure reveals that C137 is located on a central twofold axis about the dimer interface and is in a conformation compatible with disulfide bond formation. These differences are consistent with the observations that the ABC dimer interface is pH sensitive (27, 40) and that HSP27 activity shows redox dependence (46).

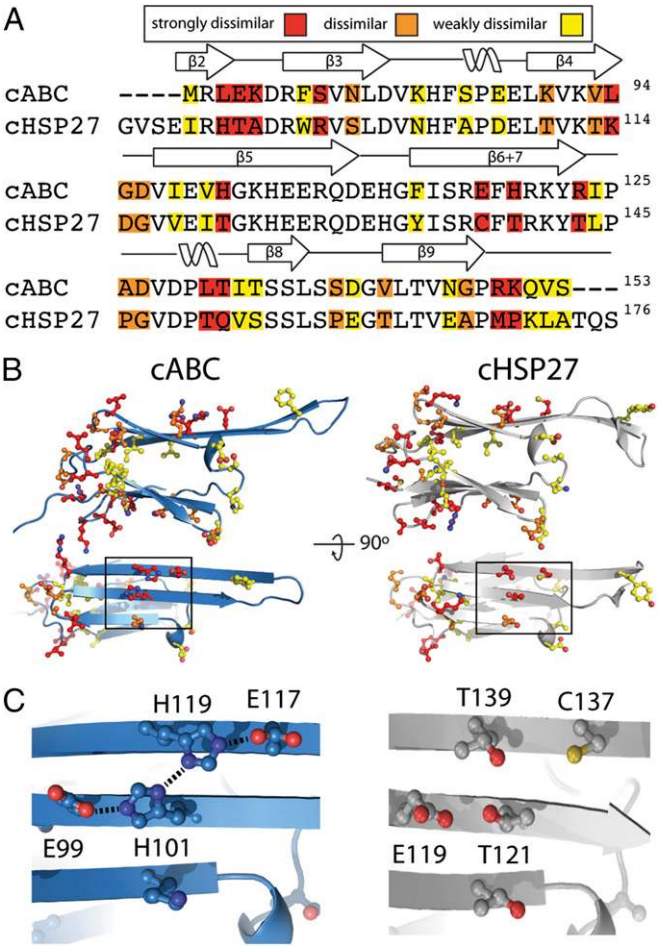

Fig. 2. Structural differences between cHSP27 and cABC. (*A*) Sequence alignment of the two domains colored to highlight differences in amino acid composition (strongly dissimilar, red; dissimilar, orange; weakly dissimilar, yellow; *Materials and Methods*). The two domains are clearly highly similar (54.7% identity), although differences are distributed throughout the sequence. (*B*) Mapping the disparate residues on the cABC (*Left*) and cHSP27 (*Right*) structures (colored as in *A*) shows that they are spread over the entire structure. (*C*) Expansions of the boxed regions in *B* reveal a charge network formed by residues E99, H101, E117, and H119 in cABC (*Left*) that is absent in cHSP27 (*Right*) where the equivalent residues are E119, T139, T121, and C137.

An AP_{II} Locked cABC Dimer. Motivated by the cHSP27 structure, we engineered a cysteine into cABC at position E117, which aligns to C137 in HSP27 (Fig. 2*A*) and is located about the twofold axis in the AP_{II} register (Fig. 1*C*). We crystallized this $cABC_{E117C}$ construct using our cocrystallization method (Table S1), revealing a fold very similar to that in cABC and comparable curvature of the dimer interface (Fig. 3*A*). However, one of the two dimers comprising the asymmetric unit was covalently locked by a disulfide bond between monomers, rendering it unable to access registers other than AP_{II} (Fig. 3*B*). The loops between the β5 and β6+7 strands (chains E and G) are disordered in the crystal lattice in the locked dimer but are ordered in the other dimer (Fig. S2*A*). There is near-perfect agreement in side-chain positions between cABC and $cABC_{E117C}$ (backbone and side-chain rmsd = 0.33 $Å^2$ comparing monomer). The two structures differ significantly only in that the β5 and β6+7 strands are elongated in the AP_{III} register of cABC. The disulfide bond in the $cABC_{E117C}$ structure does not lead to unusual torsion angles in the β-sheet around the bond, nor in the associated dihedral angles (Fig. S2*B*). Although the introduction of strain into antiparallel β-sheets by disulfide bonds between register-paired cysteines has been proposed to be a mechanism of redox regulation (47), our $cABC_{E117C}$ structure hints that redox regulation in HSP27 is achieved via another means.

cABC Predominantly Populates the AP_{II} Register. To assess whether $cABC_{E117C}$ adopts the same monomeric fold as cABC in solution, we recorded ^{1}H-^{15}NHSQC NMR spectra for both cABC and $cABC_{E117C}$ under oxidizing conditions. In both cases, well-dispersed resonances were observed indicative of a folded structure and consistent with data for similar constructs (43, 48). For most cross-peaks in the cABC spectrum, there is a corresponding cross-peak for oxidized $cABC_{E117C}$ (Fig. 3*C*). Additional cross-peaks are visible in the $cABC_{E117C}$ spectrum that likely result from differences in subunit exchange dynamics between cABC and $cABC_{E117C}$ (48). To assess the magnitude of any changes, we determined the change in cross-peak position in both the ^{1}H and ^{15}N dimension (chemical-shift perturbation, CSP) between cABC and $cABC_{E117C}$ based on a previous assignment (Fig. 3*D*) (48). In most cases the CSPs are <0.16 ppm, which is considerably smaller that those observed in experiments probing

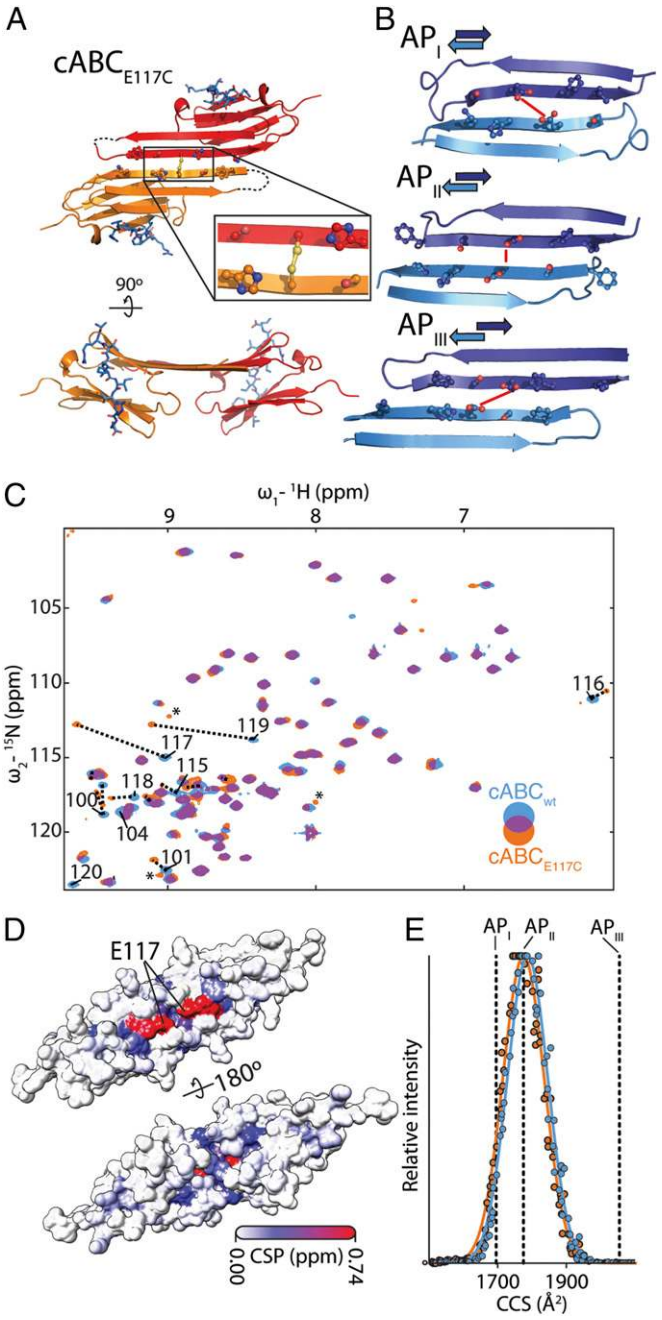

Fig. 3. NMR and IM reveal AP_{II} as the dominant registration state for cABC in solution. (*A*) Crystal structure of $cABC_{E117C}$ in which the introduced cysteine acts to lock the domain into a dimer in the AP_{II} register. The *Inset* shows the disulfide bond formed between two monomers. The overall structure of this engineered ACD is closely similar to that of cABC. (*B*) The three registers of the ABC dimer observed by X-ray crystallography: AP_I (PDB ID code: 3L1G), AP_{II} (PDB ID code: 2WJ7), and AP_{III} (PDB ID code: 4M5S). Red lines indicate the vector between α-carbons of residues E117 on the two monomers, which is located on a twofold axis in AP_{II}. The distance between two modeled cysteines at position 117 is close enough for disulfide bond formation only in AP_{II} (9.13 Å between the two thiols in AP_I, 0.93 Å in AP_{II}, and 6.5 Å in AP_{III}). (*C*) ^{1}H-^{15}*N*-HSQC spectra of cABC (blue) and $cABC_{E117C}$ (orange) acquired under identical oxidizing solution conditions. Overlap of peaks is represented by purple. Peaks with significant shifts in the mutant are labeled on the plot. Dotted lines indicate peak movement in the mutant compared with cABC, and asterisks indicate unassigned peaks. The spectra overlay very well, indicating that the fold of the two proteins is very similar. (*D*) A heat map of CSP projected onto the structure of cABC (largest CSP, red; lowest, white) reveals that the most significant changes in chemical shift are observed near C117. (*E*) IM measurements of the cABC (blue) and $cABC_{E117C}$ (orange) 7+ charge state (Fig. 4 *E* and *F*) under oxidizing conditions reveal very similar CCS distributions. Dashed lines indicate anticipated CCS values of AP_I, AP_{II}, and AP_{III}. Because the CCS distribution of cABC matches that of $cABC_{E117C}$, which is fixed as an AP_{II} dimer, we can infer that cABC preferentially populates the AP_{II} register.

the binding of ligands to a similar construct of cABC (43). The two largest CSPs (~0.7 ppm) are E117 (the site of mutation) and H119, which is hydrogen-bonded to E117 in our cABC structure. Mapping these small CSPs onto the structure of cABC shows that they cluster around the site of mutation (Fig. 3*D*), as expected because of the change in chemical environment caused by the substitution of side-chains. The monomeric folds of cABC and $cABC_{E117C}$ in solution therefore are extremely similar, despite $cABC_{E117C}$ being locked into the AP_{II} registration.

To investigate which register cABC populates at equilibrium, we used ion mobility spectrometry (IM), a technique that reports the overall size of the molecule in terms of a rotationally averaged collisional cross-section (CCS) (49). Theoretical calculations based on the crystal structures of the different forms (Fig. 3*B*) predict that AP_I and AP_{III} differ from AP_{II} in CCS by –4.5% and 15.8%, respectively (Fig. 3*E*, dashed lines). However, comparison of IM data for cABC and $cABC_{E117C}$ under oxidizing conditions reveals no noticeable differences in CCS distributions (Fig. 3*E*), even though the disulfide-locked $cABC_{E117C}$ is unable to access either AP_I or AP_{III}. This result, combined with the similarity of monomeric folds of cABC and $cABC_{E117C}$, indicates that, outside a crystal lattice, cABC exists predominantly in the AP_{II} register.

The Dynamics of $cABC_{E117C}$ Under Reducing Conditions Are Equivalent to Those of cABC. To interrogate the dynamics of cABC, we performed nanoelectrospray MS measurements under conditions that preserve noncovalent interactions in vacuo (50). A mass spectrum obtained for cABC features two charge-state distributions, centered on 2,000 *m/z* and 2,500 *m/z*, which partially overlap and correspond to monomers and dimers, respectively (Fig. 4*A*). At this concentration (8 μM, based on the molar mass of a monomer) a substantial amount of monomer is observed. Increasing the concentration of cABC to 32 μM results in an increasing abundance of dimers (Fig. 4*B*), consistent with a K_d on the order of a few micromolars (51). Under oxidizing conditions $cABC_{E117C}$ forms only dimers, in line with the formation of a disulfide bond between monomers observed in the crystal structure (Fig. 4*D*). Upon the addition of reductant, $cABC_{E117C}$ immediately reverts to a monomer–dimer equilibrium with a K_d comparable to that of cABC (Fig. 4*E*).

To characterize the kinetics of the monomer–dimer equilibrium in cABC, we performed experiments in which mass spectra of cABC and a ^{13}C-labeled equivalent were acquired as soon as possible after mixing at 4 °C. Examination of the region of the spectrum corresponding to dimers reveals $^{12}C^{12}C$- and $^{13}C^{13}C$-homodimers and $^{12}C^{13}C$-heterodimers of cABC. Notably, these three dimeric forms are observed at a ratio of 1:1:2 (Fig. 4*E*), as would be expected statistically upon complete equilibration of this equimolar mixture. As such, exchange is completed faster than the dead-time of the experiment. This timescale corresponds to a lower limit for the off-rate constant of a monomer from the dimer of 0.1/s, approximately five orders of magnitude faster than that of a monomer dissociating from an oligomer of ABC at the same temperature (27). The equivalent experiment performed for $cABC_{E117C}$ under oxidizing conditions shows no subunit exchange, even after prolonged incubation, as anticipated because of the covalent linkage between homodimers. In the presence of reductant, $cABC_{E117C}$ exchanges subunits as rapidly as cABC (Fig. 4 *D* and *F*). Combined, these results demonstrate that $cABC_{E117C}$ is a redox-sensitive protein that

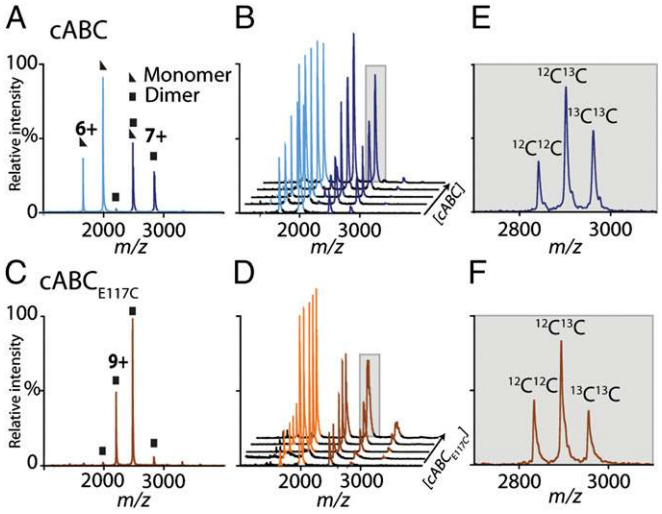

Fig. 4. Quaternary dynamics of cABC and $cABC_{E117C}$. (*A*) Nanoelectrospray MS of cABC reveals two charge-state distributions corresponding to an equilibrium of monomers (triangles) and dimers (squares). (*B*) A titration series of cABC reveals an increase in the abundance of dimer (dark blue) relative to monomer (light blue) as the concentration is increased (2, 4, 8, 16, and 32 μM, front to back). Spectra are normalized so that the most intense peak in each spectrum is equal to 100%. The shaded area indicates the 7+ charge state of the dimer. (*C*) A mass spectrum of $cABC_{E117C}$, obtained under the same conditions as for cABC in *A*, reveals the exclusive presence of dimers because of disulfide bond formation. (*D*) In the presence of reductant $cABC_{E117C}$ reverts to a concentration-dependent equilibrium of monomers (orange) and dimers (brown) (concentrations are as in *B*) (*E*) A mass spectrum of unlabeled cABC mixed with ^{13}C-labeled cABC, acquired as soon as possible, and focusing solely on the 7+ charge state (shaded in *B*). Both homo- and heterodimers are observed, indicating rapid subunit exchange. (*F*) An experiment equivalent to that in *E* carried out with $cABC_{E117C}$ under reducing conditions demonstrates fast subunit exchange as observed for cABC.

exists as a stable cross-linked dimer under oxidizing conditions and reverts immediately to a monomer–dimer equilibrium with fast subunit exchange dynamics, comparable to those of cABC, upon the addition of reductant.

cABC Can Prevent Amorphous Protein Aggregation in Vitro. The cABC system provides an excellent means to probe the chaperone activity of the core domain itself and to study the importance of the monomer–dimer equilibrium and its associated subunit-exchange dynamics. To investigate these properties, we assayed the ability of cABC, $cABC_{E117C}$, and full-length ABC to protect three very different targets: α-lactalbumin (α-lac), κ-casein, and the amyloid β-peptide ($Aβ_{1–42}$). These polypeptides differ in their amino acid sequence, molar mass, mechanism and rate of aggregation, and morphology of the resulting aggregates. To make our assays sensitive to small differences in chaperone activity, we optimized the chaperone:target molar ratios so that our assays exhibited measurable aggregation of the targets,.

We first monitored the ability of the different constructs to inhibit the reduction-induced amorphous aggregation of α-lac at 37 °C. In the absence of chaperone, after a lag phase of about 20 min, we observed a rapid increase in apparent absorbance caused by light scattering (Fig. 5*A*, red), indicating the aggregation of α-lac (52). Upon the addition of cABC, we found a considerable delay in the onset and a reduction in the rate of α-lac aggregation (Fig. 5*A*, blue). The extent of protection conferred was strongly dependent on the amount of chaperone, although significant protection ($P < 0.01$) was observed even at molar ratios of cABC:α-lac as low as 1:80. This result indicates that cABC affords potent protection against amorphous protein aggregation at substoichiometric amounts and in a dose-dependent manner.

To quantify the relative efficacy of protection relative to full-length ABC and $cABC_{E117C}$, we performed a comparative assay at a chaperone:α-lac ratio of 1:5. All three chaperones significantly delayed and slowed α-lac aggregation (Fig. 5*B*). Remarkably, comparison of cABC and full-length ABC reveals no significant difference in their activity. Notably cHSP27, despite being of similar fold to cABC, displayed minimal chaperone activity in this and other assays (Fig. S3). As such it can be regarded as a negative control and demonstrates the specificity of the chaperone action observed for the constructs of ABC.

In this assay, therefore, we found that the ACD in ABC is entirely sufficient for chaperone function (Fig. 5*B*). Notably, we observe that $cABC_{E117C}$ is more effective than cABC in preventing aggregation of α-lac. It is important to consider that the presence of DTT in this assay means that the disulfide bond in $cABC_{E117C}$ is reduced (Fig. 4*F*), so this increased activity cannot be ascribed to the exclusive presence of an AP_{II}-locked dimer. Instead we observe that $cABC_{E117C}$ displays increased binding, relative to cABC, of the hydrophobic probe bis-ANS (4,4′-dianilino-1,1′-binaphthyl-5,5′-disulfonic acid), revealing an increased solvent-accessible hydrophobic surface area (Fig. S4). The slight differences in structure between cABC and $cABC_{E117C}$ revealed by our NMR experiments (Fig. 3*D*) provide one possible rationale for the difference in chaperone activity.

cABC Can Prevent Amyloid Fibril Formation in Vitro. We next tested the ability of cABC to prevent amyloid fibril formation using two model systems: κ-casein and $Aβ_{1–42}$. In these experiments, fibril formation is assayed by monitoring the characteristic red-shift in fluorescence of the dye thioflavin T (ThT) upon binding to amyloid structures. In the absence of chaperone, κ-casein forms fibrils relatively slowly (over a period of >20 h), without a significant lag phase (Fig. 5*C*). The timescale of this aggregation is not significantly altered with the presence (Fig. 5*C*, *Upper*) or absence (Fig. 5*C*, *Lower*) of the reductant DTT. At a chaperone:κ-casein molar ratio of 1:2, ABC slows κ-casein fibril formation under both oxidizing and reducing conditions (Fig. 5*C*). At an equivalent ratio, cABC also retards amyloidogenesis and does so only slightly less effectively than the full-length protein. Notably, $cABC_{E117C}$ is more effective than cABC in slowing κ-casein aggregation. This improved activity is observed under both oxidizing and reducing conditions; in other words, it is independent of whether the chaperone is locked into AP_{II} dimers. This result suggests that the difference in activity in this case is caused by the altered surface properties of $cABC_{E117C}$ compared with cABC (Fig. 3*D* and Fig. S4), as observed in our α-lac assay (Fig. 5*B*).

To test our constructs in preventing the aggregation of a target that forms fibrils more rapidly, we assayed their ability to inhibit $Aβ_{1–42}$ amyloidogenesis. In the absence of chaperone, this peptide aggregates over a period of approximately 3 h, in both the presence and absence of DTT (Fig. 5*D*). At a chaperone:$Aβ_{1–42}$ molar ratio of 1:20 and in both conditions, we found that all three constructs dramatically slowed aggregation. Notably, no significant difference was observed for cABC relative to the full-length protein (Fig. 5*D*). Under reducing conditions (Fig. 5*D*, *Upper*) cABC and $cABC_{E117C}$ have equivalent chaperone ability in this assay. However, under oxidizing conditions (Fig. 5*D*, *Lower*) $cABC_{E117C}$ is more effective than cABC in inhibiting $Aβ_{1–42}$ fibril formation. Therefore, locking cABC into an AP_{II} dimer makes it a more potent chaperone in this assay.

The Interaction of cABC with Aggregating $Aβ_{1–42}$ Reduces Toxicity to Cells. To test whether the inhibitory effect of cABC on $Aβ_{1–42}$ amyloid formation would result in a decrease in toxicity, we performed assays on cultured cells. Specifically we monitored the viability of HEK293, HeLa, and PC12 cells upon the addition of preincubated $Aβ_{1–42}$ (Fig. 5*E*). In all three cell lines, the addition

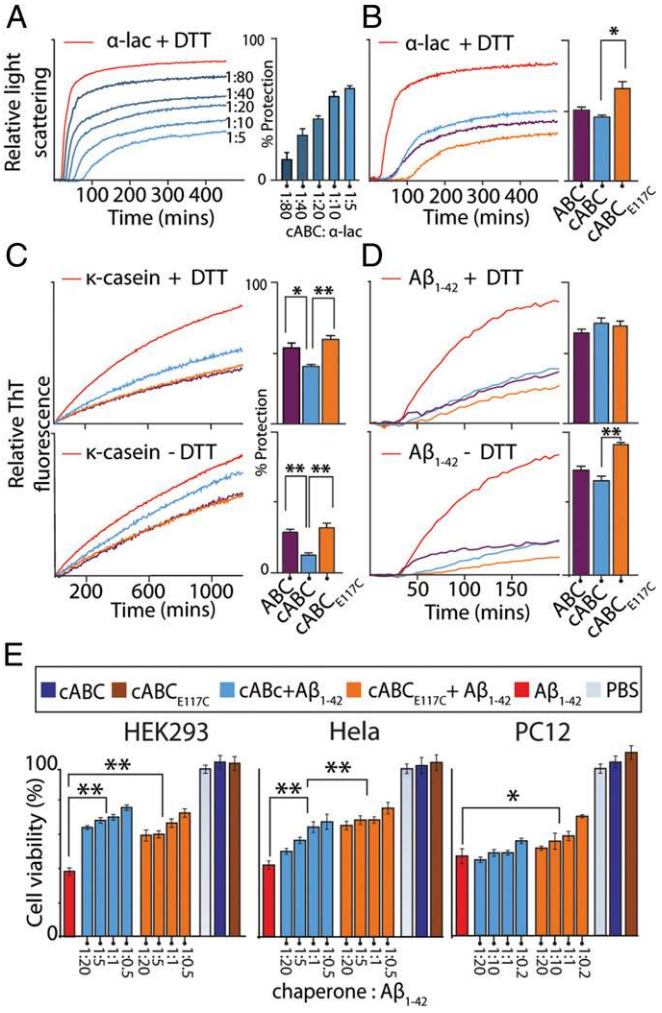

Fig. 5. In vitro chaperone activity of ACDs. (*A*) Dose-dependent inhibition of reduction-induced α-lac aggregation by cABC. Molar ratios are indicated as cABC:α-lac. Even at substoichiometric quantities of cABC, significant chaperone activity is observed. (*B*) Comparing different constructs of ABC at a molar ratio of 1:5 (chaperone:α-lac) reveals cABC to be equivalently potent to the full-length protein. cABC$_{E117C}$ is slightly more effective than cABC, likely because of altered surface properties around the introduced cysteine (Fig. S3). (*C*) Assaying κ-casein fibrillation under reducing (*Upper*) and oxidizing (*Lower*) conditions in the presence of our ABC constructs at a chaperone:κ-casein molar ratio of 1:2 demonstrates that they are capable of slowing aggregation. cABC is less efficient than the full-length protein in both conditions, whereas cABC$_{E117C}$ is more effective than cABC, mirroring the data in *B*. (*D*) The ABC constructs also are potent inhibitors of Aβ$_{1-42}$ fibrillation at a chaperone:Aβ$_{1-42}$ molar ratio of 1:20. Under reducing conditions (*Upper*), all three constructs perform equivalently, but under oxidizing conditions (*Lower*), cABC$_{E117C}$ is more effective than cABC. This result suggests that locking into an AP$_{II}$ dimer improves chaperone action in this assay. In all cases (*A*–*D*), a representative aggregation assay is shown as well as the percentage protection. Error bars correspond to mean ± SEM, with $n = 3$. $^*P < 0.05$, $^{**}P < 0.01$. (*E*) Cell-viability assays upon the addition of Aβ$_{1-42}$ to HEK293, HeLa, and PC12 cells. Aβ$_{1-42}$ on its own (red) decreases viability to 40%, but cABC (dark blue), cABC$_{E117C}$ (brown), and buffer (gray) have no effect. Aβ$_{1-42}$ incubated in the presence of increasing amounts of cABC (blue) and cABC$_{E117C}$ (orange) is less toxic than in the absence of chaperone. Molar ratios indicated are chaperone:Aβ$_{1-42}$, with an Aβ$_{1-42}$ concentration of 0.5 μM in all experiments (except the controls without Aβ$_{1-42}$). In all cases chaperone protection is clearly dependent on concentration. Error bars correspond to mean ± SEM, with $n = 4$. $^*P < 0.05$.

of Aβ$_{1-42}$ decreased viability to about 40%, indicating toxicity of the aggregating peptide. The addition of solutions of Aβ$_{1-42}$ that had been incubated in the presence of chaperone reduced this toxicity. Notably, not all cell lines responded equivalently; both cABC and cABC$_{E117C}$ rescued HEK293 and HeLa cells more effectively than PC12 cells. Although the reasons for this are not known, it is clear that the protective effect was more pronounced with increasing ratios of chaperone:Aβ$_{1-42}$, demonstrating a dose-dependency in all cases. This result mirrors data obtained for full-length ABC (19, 20) and reveals that the ACD is sufficient to slow the rate of Aβ$_{1-42}$ aggregation and thereby reduce the toxicity of the aggregating mixture. Interestingly, in these assays, which are performed in the absence of reductant, we detect a clear increase in potency for cABC$_{E117C}$ relative to cABC in HeLa cells, and in PC12 cells only cABC$_{E117C}$ displayed statistically significant potency. This result implies that locking cABC into an AP$_{II}$ dimer, which improves its efficacy in slowing the rate of Aβ$_{1-42}$ in vitro (Fig. 5*D*, *Lower*), results in an associated reduction in toxicity of the aggregating mixture.

Discussion

We have found that the core domain of ABC is a potent inhibitor of both amorphous and fibrillar aggregation and of amyloid-associated toxicity. Previous reports describing alternatively truncated forms of ABC have shown limited chaperone activity toward other target proteins (41, 53). However, our construct performed comparably to full-length ABC in protecting α-lac and κ-casein from aggregation at substoichiometric levels. Remarkably, our amyloidogenesis and cell toxicity assays of Aβ$_{1-42}$ places cABC among the most potent known inhibitors of Aβ$_{1-42}$ on a molar basis (54). The finding that the ACD can prevent amyloid formation and toxicity is surprising and raises questions about the role of its flanking and relatively unstructured N- and C- terminal regions and about the necessity of the oligomeric form of ABC.

It is important to recognize that our assays report primarily on the ability of the ACD to delay aggregation and not on the stability of any complexes formed or on their interactions with the cellular disaggregation, refolding, or degradation machinery (10, 55). Similarly, we probed only the chaperone function of ABC against selected targets; it is known that the chaperone has other important roles, including being a major structural component of the eye lens, which may require oligomerization (56). It is interesting that chaperone activity of dimeric sHSPs has been reported from various organisms, including HSP17.7 from *Deinococcus radiodurans* (57), HSP18.5 from *Arabidopsis thaliana* (58), and human HSP20 (59). Although these chaperones do not assemble into oligomers, they still have intact N and C termini. Our results clearly demonstrate that the ACD itself can be sufficient for chaperone activity and is not simply a passive building block of sHSP oligomers.

We have shown that, against all target proteins tested, cABC$_{E117C}$ locked into an AP$_{II}$ dimer was at least as active as cABC. This result demonstrates that dissociation into monomers, subunit exchange dynamics, or accessing other dimer registration states (AP$_{I}$ or AP$_{III}$) is not a prerequisite for the chaperone function of ABC. This observation is consistent with measurements made on an equivalent E117C mutation in full-length ABC, which had activity comparable to the wild-type in preventing rhodanese from aggregating (44). Furthermore, in all our experiments the concentration of chaperone used was close to the K_d of the cABC dimer interface, meaning that a sizeable proportion of the chaperone was monomeric (51). In the case of α-lac and Aβ$_{1-42}$ this preponderance of monomer did not impair chaperone activity, suggesting that the monomeric ACD is itself chaperone-active. This notion is consistent with the observation that monomers are the exchanging unit in ABC (27). When these results are taken together with the observation that full-length ABC prevents aggregation, including when cross-linked to prevent its dissociation (36), a picture emerges in which the ACD is

chaperone-active and its binding surfaces are accessible, irrespective of its quaternary state.

Hydrophobic interactions are often hypothesized to be the likely mode of chaperone–target interactions (5, 6). Interestingly, cABC has few exposed hydrophobic patches and has fewer than the structurally similar but inactive cHSP27 (Fig. S4). Although we did measure an increase in exposed hydrophobic surface area in $cABC_{E117C}$ relative to cABC (Fig. S4), we did not detect major structural distortions in the monomeric fold caused by the mutation in either our NMR or X-ray crystallography experiments. Therefore it is possible that the increased chaperone activity of $cABC_{E117C}$ may be caused by residue 117 being proximal to the binding site of cABC and the mutation to cysteine resulting in favorable changes to the protein surface. Alternatively, we have established previously that the dimer interface and the β4–β8 groove that accommodates the C-terminal peptide are allosterically coupled: the strengthening of one results in the weakening of the other (27, 51). It is possible that stabilizing the dimer interface through the covalent linkage may increase the accessibility of the groove as a potential site for target binding.

Although cABC is an effective chaperone against the aggregation of all the targets assayed here, there nonetheless remain differences in the effectiveness of protection provided by cABC and that provided by full-length ABC. In the case of α-lac, the core is entirely sufficient for chaperone function, but with κ-casein it is somewhat less active than full-length ABC. The effect of the E117C mutation resulted in an increase in potency against α-lac and κ-casein regardless of its redox state (Fig. S4). Interestingly, $cABC_{E117}$ also was more potent than cABC against $A\beta_{1–42}$ aggregation, but only when the disulfide bond locked $cABC_{E117}$ into a dimeric form. Combined, these observations suggest there are subtle differences in the way the ACD interacts with different targets, perhaps through separate parts of its molecular surface. This notion is consistent with observations of different modes of action for amorphous and amyloidogenic aggregation (60, 61) and for chaperone activity for peptides from different regions of ABC (31, 32).

It is important to note that sequence differences between cABC and the chaperone-inactive cHSP27 are distributed all over the surface and do not cluster around either the dimer interface or the β4–β8 groove (Fig. 2). The small number of differences in primary amino acid sequence therefore does not point to any particular patch of the domain that renders cABC active and cHSP27 inactive. Irrespective of the exact location of the binding site on cABC, the similarity of the cABC and cHSP27 structures suggests that specific residues mediate the interaction between cABC and the targets assayed here. Importantly, the system and approaches we have developed will enable us to probe structurally this important function of sHSP. Understanding how such a small folded protein inhibits amyloid toxicity may be of great use in the search for effective biotherapeutic strategies for diseases associated with amyloid fibril formation.

Materials and Methods

ABC, cABC, and cHSP27 Protein Expression and Purification. Human ABC, cABC (residues 68–153), and cHSP27 (residues 84–176) were cloned, expressed, and purified as described previously (41, 51), with the exception that in the His-tag buffers phosphate was replaced by Tris. Truncated proteins were expressed with N-terminal tobacco etch virus (TEV) protease-cleavable His-tags and purified by using nickel-affinity chromatography. The N-terminal His-tag was removed with TEV protease, and the protein buffer was exchanged using either a Superdex 75 gel filtration column (GE Healthcare) or two 5-mL HiTrap desalting columns (GE Healthcare) connected in series. For subunit exchange experiments, cABC was expressed in M9 minimal medium containing ^{13}C-labeled D-glucose as the only carbon source and was purified as described above. For NMR experiments, cABC and $cABC_{E117C}$ were expressed in M9 minimal medium containing ^{15}N ammonium chloride as the only nitrogen source.

ABC and HSP27 C-Terminal Peptide Expression and Purification. The C-terminal peptides (ABC residues 156–164, ERTIPITRE; HSP27 residues 179–185, ITIPVTF) were purchased (Biomatik or Genscript) or were expressed recombinantly and purified as described previously (62). Briefly, an expression construct containing an N-terminal His-tagged maltose-binding protein followed by a TEV protease cleavage site in pET15b (Novagen) was amplified by PCR using a T7 forward primer and reverse primer with a 5′ overhang containing the DNA sequence for the C-terminal peptide followed by a stop codon and XhoI restriction site. The subsequent PCR product was digested with NdeI and XhoI (New England Biolabs) followed by ligation using a Quick Ligation kit (New England Biolabs) into pET28b. The fusion construct was expressed and purified using nickel-affinity chromatography followed by TEV protease cleavage, leaving an additional N-terminal glycine, and purification using reverse-phase HPLC. Peptide fractions were verified by MS and were stored in desiccant jars at −20 °C.

Crystallization of cABC and cHSP27 in Complex with their C-Terminal Peptides. Crystals were grown in hanging-drop plates (VDX; Hampton Research) at room temperature. A final mixture containing 8–10 mg/mL monomer supplemented with a two- to threefold molar excess of the appropriate C-terminal peptide (10 mM stock, in water) was prepared in X-tal buffer [100 mM sodium chloride, 20 mM Tris (pH 8.0)]. Crystals of cABC with recombinant C-terminal peptide grew in 0.1 M SPG (succinic acid, dihydrogen phosphate, glycine) buffer, pH 6.0, and 25% (vol/vol) PEG 1500. Crystals of $cABC_{E117C}$ with synthetic C-terminal peptide grew in 0.085 M Mes (pH 6.5), 0.17 M ammonium sulfate, 25.5% (vol/vol) PEG 5000 monomethyl ether, and 15% (vol/vol) glycerol. A final mixture containing 9 mg/mL cHSP27 supplemented with a twofold molar excess of the synthetic C-terminal peptide (10 mM stock, in water) prepared in Xtal buffer supplemented with 1 mM DTT was crystallized in Crystal Screen (Hampton Research) condition no. 6 [0.2 M magnesium chloride, 0.1 M Tris (pH 8.5), and 30% (vol/vol) PEG 4,000]. With the exception of $cABC_{E117C}$, crystals were cryo-protected in mother-liquid solution containing 20% (vol/vol) glycerol. All crystals were flash-frozen in liquid nitrogen.

Structure Determination and Analysis. X-ray diffraction data were processed using XDS (63), and structures were determined by molecular replacement using Phaser (64), followed by automated model building using Phenix (65). Models were built using Coot (66) and refined with REFMAC (67), Phenix (65), and Buster (68). Structures of cABC, $cABC_{E117C}$, and cHSP27 have been deposited in the RCSB PDB with the ID codes 4M5S, 4M5T, and 4MJH, respectively.

Buried surface areas in the dimer interface were calculated using the PISA server (69). 3L1G and 2WJ7 were used for calculations for AP_I and AP_{II}. Sequence alignments were generated using the ClustalW2 server (70). Amino acids were colored according to their score in the Gonnet Pam250 matrix generated by the ClustalW2 server (<0: red; ≤0.5: orange, >0.5: yellow), and fully conserved residues were not colored (Fig. 2*A*). Surface hydrophobicity was calculated and rendered using the University of California, San Franciso Chimera (71).

MS. MS measurements were carried out on a IM QToF (Synapt G1; Waters) modified to incorporate a linear drift tube (72). Nanoelectrospray mass spectra were acquired under conditions optimized for the preservation of noncovalent interactions essentially as described previously (51) and with the following instrument parameters: sample cone, 10 V; extraction cone, 5 V; trap, 10 V; trap gas (argon), 2.6 mL/min; drift-cell pressure (helium), 2.14 Torr. Unless stated otherwise, samples were analyzed at monomeric concentrations of 10–20 μM in 200 mM ammonium acetate (pH 6.9). DTT, to a final concentration of 5 mM, was added where stated. For subunit exchange experiments, ^{13}C-labeled and unlabeled protein was mixed at equimolar ratios at 4 °C and analyzed by MS as soon as possible after mixing (<1 min). CCSs were measured by mixing oxidized $cABC_{E11C}$ and ^{13}C-labeled cABC and then recording spectra at nine drift voltages in the range of 50–200 V. At each drift voltage, arrival times were fitted to normal distributions, and the transport time (T_0) of ions from the exit of the drift-tube region to the time-of-flight analyzer were obtained (72). CCS distributions were obtained from the arrival time (T_a) distributions of the 7+ charge state at each drift voltage, V_D, using $CCS = 4.482 \times 10^{-3}(T_a - T_o)V_D zTP^{-1}$ where z is the charge of the ion, T is the temperature in K, P the pressure in Torr, and the constant amalgamates the length of the drift tube with the necessary components of the Mason–Schamp equation (49, 72). The data from all drift voltages were combined and fitted globally to a normal distribution. Theoretical CCSs of AP_I-AP_{III} were calculated from the cABC crystal structure using CCSCalc (Waters) with a gas radius of 1 Å and tolerance of 0.1% and were normalized to the experimentally determined CCS value of AP_{II} for comparison.

NMR. NMR experiments were performed on a 600 MHz spectrometer (Varian) equipped with a 5-mm *z*-axis gradient triple-resonance probe. ^{15}N-labeled cABC and $cABC_{E117C}$ were prepared in 25 mM sodium phosphate, 2 mM EDTA, 2 mM sodium azide (pH 7.5) and concentrated to 500 μM using Amicon concentrators (Millipore). 2D ^{15}N-^{1}H HSQC correlation spectra were recorded with eight scans per transient with acquisition times (t_1, t_1) of (65.8, 135.1) ms, over (608, 100) complex points and a 1-s relaxation delay, for a total acquisition time of 26 min. All spectra were analyzed using NMRPipe (73) and Sparky (T. D. Goddard and D. G. Kneller, University of California, San Francisco). Peaks were ascribed to particular residues based on the previous assignment of a similar construct (48). To measure CSPs in both dimensions, the chemical shift difference in the nitrogen dimension was divided by 5 to account for the distribution of shifts recorded in the Biological Magnetic Resonance Bank. In the few cases where several peaks could not be clearly assigned in the $cABC_{E117C}$ spectrum, the furthest peak was used for CSP calculations to avoid underestimating the CSP. When the closest peak was used instead, the pattern of CSPs was very similar, although they were slightly smaller (Fig. S2 *C* and *D*).

In Vitro Protein Aggregation Assays. The aggregation and precipitation of the target proteins, reported via either ThT fluorescence or light-scattering assays, was monitored by using sealed 96-microwell plates and a Fluostar Optima plate reader (BMG Lab Technologies). The amorphous aggregation of α-lac (Sigma-Aldrich, 100 μM), incubated at 37 °C in 50 mM phosphate buffer containing 100 mM NaCl and 5 mM EDTA (pH 7.0), was initiated by the addition of DTT (20 mM). Chaperones were added at the molar ratios stated. Aggregation was monitored by measuring the change in apparent absorbance caused by light scattering at 340 nm, which was negligible in the absence of α-lac. The formation of amyloid fibrils by target proteins was monitored using an in situ ThT-binding assay (61). κ-casein (50 μM; Sigma-Aldrich) was incubated at 37 °C in 50 mM phosphate buffer (pH 7.4) and $A\beta_{1-42}$ (10 μM; Anaspec) at 37 °C in PBS (pH 7.4). Chaperones and DTT (20 mM) were added where stated at a chaperone:κ-casein molar ratio of 1:2 or a chaperone:$A\beta_{1-42}$ratio of 1:20. Samples were incubated with 10 μM ThT, and the fluorescence levels were measured with a 440/490 nm excitation/emission filter set. The change in ThT fluorescence in the absence of either κ-casein or $A\beta_{1-42}$ was negligible for each assay. In all cases, the relative ability of each chaperone to prevent aggregation was evaluated by comparing the apparent absorbance/ThT fluorescence at the end of each assay, as previously described (74). Data are reported as mean ± SEM ($n = 3$) and were analyzed by one-way ANOVA and Tukey's post hoc test. To assay exposed hydrophobicity, samples were prepared at 2.5 μM in PBS, and bis-ANS was added to a final concentration of 10 μM. Fluorescence spectra were recorded as previously described (60).

Cell Viability Assays. Cell viability was measured by using a CellTiter 96 aqueous nonradioactive cell proliferation assay kit (Promega #G4100). PC-12 [American Type Culture Collection (ATCC) catalog no. CRL-1721], HeLa, and HEK293 cell lines were used to assess the inhibition of our ABC constructs on $A\beta_{1-42}$ toxicity. HeLa and HEK293 cells were cultured in DMEM with 10% (vol/vol) FBS. PC12 cells were cultured in ATCC-formulated RPMI medium 1640 (ATCC) with 10% (vol/vol) heat-inactivated horse serum and 5% (vol/vol) FBS. All cells were maintained at 5% CO_2 at 37 °C. For cell-viability measurements, HeLa, HEK293, and PC-12 cells were plated out in 96-well plates (Costar) at 10,000 cells per well and were cultured for 20 h at 37 °C in 5% CO_2 before different incubation mixtures were added. These were prepared to a final concentration of 5 μM $A\beta_{1-42}$ monomer in PBS (pH 7.4), in the presence or absence of chaperone as indicated, and were incubated at 37 °C for 18 h. Then 10 μL of incubated sample was added to each well containing 90 μL cell suspension. After 24 h incubation, 15 μL dye solution was added to each well, and the cells were incubated for a further 4 h before the addition of 100 μL solution/stop mix to each well. After incubation at room temperature for 12 h, the absorbance of each well was measured at 570 nm, with the background absorbance recorded at 700 nm. The final data were normalized by using the buffer-treated cell as 100% viability and the 0.2% SDS-treated cell as 0% viability. Data are reported as mean ± SEM ($n = 4$), and the titration series were analyzed globally using an unpaired Student's t-test. Specifically, the plateau of viability at high ratios of chaperone:$A\beta_{1-42}$ was determined by fitting the data to an exponential rise to maximum (75) and was compared with the absence of chaperone altogether.

ACKNOWLEDGMENTS. G.K.A.H. is supported by an Engineering and Physical Sciences Research Council studentship held at the Systems Biology Doctoral Training Centre. H.E. is supported by an Australian Research Council Future Fellowship (FT110100586) and by a seed grant from the Australian Department of Health and Ageing. D. Cox is supported by an Australian postgraduate award. M.P.C. was supported by a National Scholarship from the University of Alabama at Birmingham for a summer internship. A.J.B. holds a David Phillip's Fellowship of the Biotechnology and Biological Sciences Research Council. C.V.R. is a Royal Society Professor. D.S.E. was supported by National Science Foundation Grant NSF-MCB-095811 and National Institutes of Health Grant AG029430. J.L.P.B. is a Royal Society University Research Fellow. A.L. is a Nicholas Kurti Junior Research Fellow of Brasenose College, Oxford.

1. Baldwin AJ, et al. (2011) Metastability of native proteins and the phenomenon of amyloid formation. *J Am Chem Soc* 133(36):14160–14163.
2. Olzscha H, et al. (2011) Amyloid-like aggregates sequester numerous metastable proteins with essential cellular functions. *Cell* 144(1):67–78.
3. Powers ET, Balch WE (2013) Diversity in the origins of proteostasis networks–a driver for protein function in evolution. *Nat Rev Mol Cell Biol* 14(4):237–248.
4. Balch WE, Morimoto RI, Dillin A, Kelly JW (2008) Adapting proteostasis for disease intervention. *Science* 319(5865):916–919.
5. Hartl FU, Bracher A, Hayer-Hartl M (2011) Molecular chaperones in protein folding and proteostasis. *Nature* 475(7356):324–332.
6. Richter K, Haslbeck M, Buchner J (2010) The heat shock response: Life on the verge of death. *Mol Cell* 40(2):253–266.
7. Basha E, O'Neill H, Vierling E (2012) Small heat shock proteins and α-crystallins: Dynamic proteins with flexible functions. *Trends Biochem Sci* 37(3):106–117.
8. Hilton GR, Lioe H, Stengel F, Baldwin AJ, Benesch JLP (2013) Small heat-shock proteins: Paramedics of the cell. *Top Curr Chem* 328:69–98.
9. McHaourab HS, Godar JA, Stewart PL (2009) Structure and mechanism of protein stability sensors: Chaperone activity of small heat shock proteins. *Biochemistry* 48(18): 3828–3837.
10. Carra S, et al. (2013) Different anti-aggregation and pro-degradative functions of the members of the mammalian sHSP family in neurological disorders. *Philos Trans R Soc Lond B Biol Sci* 368(1617):20110409.
11. Garrido C, Paul C, Seigneuric R, Kampinga HH (2012) The small heat shock proteins family: The long forgotten chaperones. *Int J Biochem Cell Biol* 44(10):1588–1592.
12. Horwitz J (1992) Alpha-crystallin can function as a molecular chaperone. *Proc Natl Acad Sci USA* 89(21):10449–10453.
13. Boncoraglio A, Minoia M, Carra S (2012) The family of mammalian small heat shock proteins (HSPBs): Implications in protein deposit diseases and motor neuropathies. *Int J Biochem Cell Biol* 44(10):1657–1669.
14. Ecroyd H, Carver JA (2009) Crystallin proteins and amyloid fibrils. *Cell Mol Life Sci* 66 (1):62–81.
15. Kampinga HH, Garrido C (2012) HSPBs: Small proteins with big implications in human disease. *Int J Biochem Cell Biol* 44(10):1706–1710.
16. Chiti F, Dobson CM (2006) Protein misfolding, functional amyloid, and human disease. *Annu Rev Biochem* 75:333–366.
17. Eisenberg D, Jucker M (2012) The amyloid state of proteins in human diseases. *Cell* 148(6):1188–1203.
18. Haass C, Selkoe DJ (2007) Soluble protein oligomers in neurodegeneration: Lessons from the Alzheimer's amyloid beta-peptide. *Nat Rev Mol Cell Biol* 8(2):101–112.
19. Wilhelmus MM, et al. (2006) Small heat shock proteins inhibit amyloid-beta protein aggregation and cerebrovascular amyloid-beta protein toxicity. *Brain Res* 1089(1): 67–78.
20. Mannini B, et al. (2012) Molecular mechanisms used by chaperones to reduce the toxicity of aberrant protein oligomers. *Proc Natl Acad Sci USA* 109(31):12479–12484.
21. Knowles TP, et al. (2007) Kinetics and thermodynamics of amyloid formation from direct measurements of fluctuations in fibril mass. *Proc Natl Acad Sci USA* 104(24): 10016–10021.
22. Raman B, et al. (2005) AlphaB-crystallin, a small heat-shock protein, prevents the amyloid fibril growth of an amyloid beta-peptide and beta2-microglobulin. *Biochem J* 392(Pt 3):573–581.
23. Rekas A, et al. (2004) Interaction of the molecular chaperone alphaB-crystallin with alpha-synuclein: Effects on amyloid fibril formation and chaperone activity. *J Mol Biol* 340(5):1167–1183.
24. Shammas SL, et al. (2011) Binding of the molecular chaperone αB-crystallin to Aβ amyloid fibrils inhibits fibril elongation. *Biophys J* 101(7):1681–1689.
25. Waudby CA, et al. (2010) The interaction of alphaB-crystallin with mature alpha-synuclein amyloid fibrils inhibits their elongation. *Biophys J* 98(5):843–851.
26. Binger KJ, et al. (2013) Avoiding the oligomeric state: αB-crystallin inhibits fragmentation and induces dissociation of apolipoprotein C-II amyloid fibrils. *FASEB J* 27 (3):1214–1222.
27. Baldwin AJ, Lioe H, Robinson CV, Kay LE, Benesch JLP (2011) αB-crystallin polydispersity is a consequence of unbiased quaternary dynamics. *J Mol Biol* 413(2):297–309.
28. Aquilina JA, Shrestha S, Morris AM, Ecroyd H (2013) Structural and functional aspects of hetero-oligomers formed by the small heat shock proteins αB-crystallin and HSP27. *J Biol Chem* 288(19):13602–13609.
29. Delbecq SP, Klevit RE (2013) One size does not fit all: The oligomeric states of αB crystallin. *FEBS Lett* 587(8):1073–1080.
30. Aquilina JA, Watt SJ (2007) The N-terminal domain of alphaB-crystallin is protected from proteolysis by bound substrate. *Biochem Biophys Res Commun* 353(4): 1115–1120.

31. Bhattacharyya J, Padmanabha Udupa EG, Wang J, Sharma KK (2006) Mini-alphaB-crystallin: A functional element of alphaB-crystallin with chaperone-like activity. *Biochemistry* 45(9):3069–3076.
32. Ghosh JG, Estrada MR, Clark JI (2005) Interactive domains for chaperone activity in the small heat shock protein, human alphaB crystallin. *Biochemistry* 44(45):14854–14869.
33. Narayanan S, Kamps B, Boelens WC, Reif B (2006) alphaB-crystallin competes with Alzheimer's disease beta-amyloid peptide for peptide-peptide interactions and induces oxidation of Abeta-Met35. *FEBS Lett* 580(25):5941–5946.
34. Sharma KK, Kaur H, Kester K (1997) Functional elements in molecular chaperone alpha-crystallin: Identification of binding sites in alpha B-crystallin. *Biochem Biophys Res Commun* 239(1):217–222.
35. Bova MP, Ding LL, Horwitz J, Fung BKK (1997) Subunit exchange of alphaA-crystallin. *J Biol Chem* 272(47):29511–29517.
36. Augusteyn RC (2004) Dissociation is not required for alpha-crystallin's chaperone function. *Exp Eye Res* 79(6):781–784.
37. Aquilina JA, et al. (2005) Subunit exchange of polydisperse proteins: Mass spectrometry reveals consequences of alphaA-crystallin truncation. *J Biol Chem* 280(15): 14485–14491.
38. Bagnéris C, et al. (2009) Crystal structures of alpha-crystallin domain dimers of alphaB-crystallin and Hsp20. *J Mol Biol* 392(5):1242–1252.
39. Clark AR, Naylor CE, Bagnéris C, Keep NH, Slingsby C (2011) Crystal structure of R120G disease mutant of human αB-crystallin domain dimer shows closure of a groove. *J Mol Biol* 408(1):118–134.
40. Jehle S, et al. (2010) Solid-state NMR and SAXS studies provide a structural basis for the activation of alphaB-crystallin oligomers. *Nat Struct Mol Biol* 17(9):1037–1042.
41. Laganowsky A, et al. (2010) Crystal structures of truncated alphaA and alphaB crystallins reveal structural mechanisms of polydispersity important for eye lens function. *Protein Sci* 19(5):1031–1043.
42. Laganowsky A, Eisenberg D (2010) Non-3D domain swapped crystal structure of truncated zebrafish alphaA crystallin. *Protein Sci* 19(10):1978–1984.
43. Delbecq SP, Jehle S, Klevit R (2012) Binding determinants of the small heat shock protein, αB-crystallin: Recognition of the 'IxI' motif. *EMBO J* 31(24):4587–4594.
44. Mymrikov EV, Bukach OV, Seit-Nebi AS, Gusev NB (2010) The pivotal role of the beta 7 strand in the intersubunit contacts of different human small heat shock proteins. *Cell Stress Chaperones* 15(4):365–377.
45. Baranova EV, et al. (2011) Three-dimensional structure of α-crystallin domain dimers of human small heat shock proteins HSPB1 and HSPB6. *J Mol Biol* 411(1):110–122.
46. Arrigo AP (2001) Hsp27: Novel regulator of intracellular redox state. *IUBMB Life* 52(6): 303–307.
47. Indu S, Kochat V, Thakurela S, Ramakrishnan C, Varadarajan R (2011) Conformational analysis and design of cross-strand disulfides in antiparallel β-sheets. *Proteins* 79(1): 244–260.
48. Jehle S, et al. (2009) alphaB-crystallin: A hybrid solid-state/solution-state NMR investigation reveals structural aspects of the heterogeneous oligomer. *J Mol Biol* 385(5):1481–1497.
49. Ruotolo BT, Benesch JLP, Sandercock AM, Hyung SJ, Robinson CV (2008) Ion mobility-mass spectrometry analysis of large protein complexes. *Nat Protoc* 3(7):1139–1152.
50. Benesch JLP, Ruotolo BT (2011) Mass spectrometry: Come of age for structural and dynamical biology. *Curr Opin Struct Biol* 21(5):641–649.
51. Hilton GR, et al. (2013) C-terminal interactions mediate the quaternary dynamics of αB-crystallin. *Philos Trans R Soc Lond B Biol Sci* 368(1617):20110405.
52. Carver JA, et al. (2002) The interaction of the molecular chaperone α-crystallin with unfolding α-lactalbumin: A structural and kinetic spectroscopic study. *J Mol Biol* 318(3):815–827.
53. Feil IK, Malfois M, Hendle J, van Der Zandt H, Svergun DI (2001) A novel quaternary structure of the dimeric alpha-crystallin domain with chaperone-like activity. *J Biol Chem* 276(15):12024–12029.
54. Härd T, Lendel C (2012) Inhibition of amyloid formation. *J Mol Biol* 421(4-5):441–465.
55. Liberek K, Lewandowska A, Zietkiewicz S (2008) Chaperones in control of protein disaggregation. *EMBO J* 27(2):328–335.
56. Piatigorsky J, Wistow G (1991) The recruitment of crystallins: New functions precede gene duplication. *Science* 252(5009):1078–1079.
57. Bepperling A, et al. (2012) Alternative bacterial two-component small heat shock protein systems. *Proc Natl Acad Sci USA* 109(50):20407–20412.
58. Basha E, et al. (2013) An unusual dimeric small heat shock protein provides insight into the mechanism of this class of chaperones. *J Mol Biol* 425(10):1683–1696.
59. Bukach OV, Seit-Nebi AS, Marston SB, Gusev NB (2004) Some properties of human small heat shock protein Hsp20 (HspB6). *Eur J Biochem* 271(2):291–302.
60. Kulig M, Ecroyd H (2012) The small heat-shock protein αB-crystallin uses different mechanisms of chaperone action to prevent the amorphous versus fibrillar aggregation of α-lactalbumin. *Biochem J* 448(3):343–352.
61. Ecroyd H, et al. (2008) Dissociation from the oligomeric state is the rate-limiting step in fibril formation by kappa-casein. *J Biol Chem* 283(14):9012–9022.
62. Laganowsky A, et al. (2012) Atomic view of a toxic amyloid small oligomer. *Science* 335(6073):1228–1231.
63. Kabsch W (1993) Automatic processing of rotation diffraction data from crystals of initially unknown symmetry and cell constants. *J Appl Cryst* 26(6):795–800.
64. McCoy AJ, et al. (2007) Phaser crystallographic software. *J Appl Cryst* 40(Pt 4):658–674.
65. Adams PD, et al. (2002) PHENIX: Building new software for automated crystallographic structure determination. *Acta Crystallogr D Biol Crystallogr* 58(Pt 11): 1948–1954.
66. Emsley P, Lohkamp B, Scott WG, Cowtan K (2010) Features and development of Coot. *Acta Crystallogr D Biol Crystallogr* 66(Pt 4):486–501.
67. Murshudov GN, Vagin AA, Dodson EJ (1997) Refinement of macromolecular structures by the maximum-likelihood method. *Acta Crystallogr D Biol Crystallogr* 53(Pt 3): 240–255.
68. Smart OS, et al. (2012) Exploiting structure similarity in refinement: Automated NCS and target-structure restraints in BUSTER. *Acta Crystallogr D Biol Crystallogr* 68(Pt 4): 368–380.
69. Krissinel E, Henrick K (2007) Inference of macromolecular assemblies from crystalline state. *J Mol Biol* 372(3):774–797.
70. Larkin MA, et al. (2007) Clustal W and Clustal X version 2.0. *Bioinformatics* 23(21): 2947–2948.
71. Pettersen EF, et al. (2004) UCSF Chimera—a visualization system for exploratory research and analysis. *J Comput Chem* 25(13):1605–1612.
72. Bush MF, et al. (2010) Collision cross sections of proteins and their complexes: A calibration framework and database for gas-phase structural biology. *Anal Chem* 82(22):9557–9565.
73. Delaglio F, et al. (1995) NMRPipe: A multidimensional spectral processing system based on UNIX pipes. *J Biomol NMR* 6(3):277–293.
74. Ecroyd H, Carver JA (2008) The effect of small molecules in modulating the chaperone activity of alphaB-crystallin against ordered and disordered protein aggregation. *FEBS J* 275(5):935–947.
75. Slob W (2002) Dose-response modeling of continuous endpoints. *Toxicol Sci* 66(2): 298–312.

Supporting Information

Hochberg et al. 10.1073/pnas.1322673111

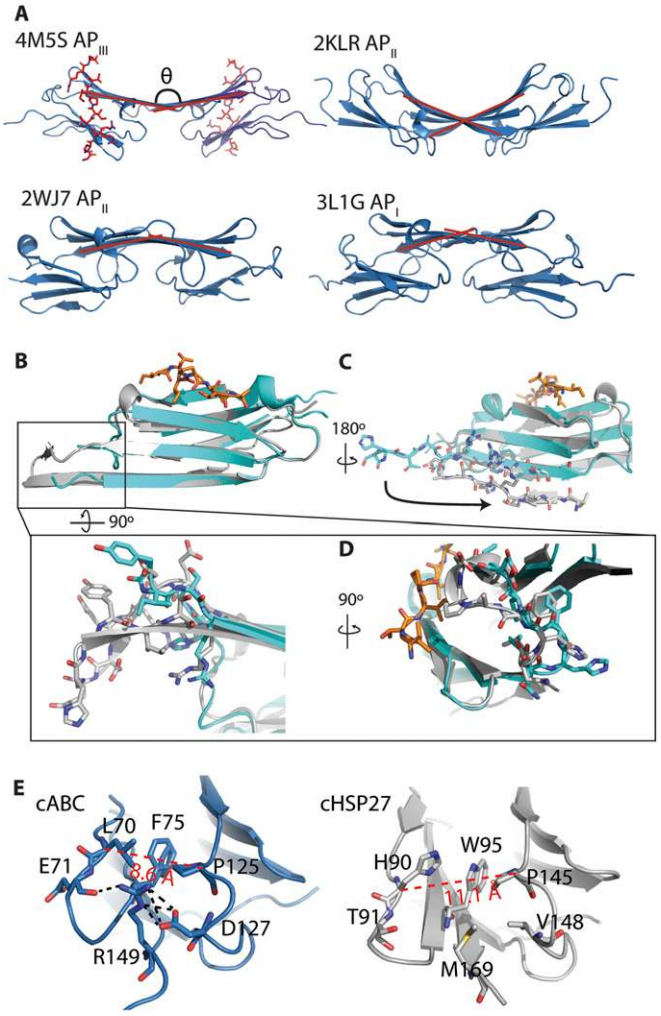

Fig. S1. (*A*) Comparison of X-ray and solid-state NMR structures of small heat-shock protein (sHSP) α-crystallin domain (ACD) structures. The solid-state NMR structure of αB-crystallin (ABC) [Protein Data Bank (PDB) ID code: 2KLR] has a bent dimer interface, which is partly mirrored in our AP_{III} structure [Research Collaboratory for Structural Bioinformatics (RCSB) PDB ID: 4M5S]. AP_{II} (PDB ID code: 2WJ7) and AP_{I} (PDB ID code: 3L1G) crystal structures show flatter dimer interfaces. Red lines indicate the angle θ between the two β-strands forming the dimer interface. (*B*) Overlay of our cHSP27 structure (RCSB PDB ID 4MJH, gray) and peptide in orange with a previous structure that crystallized as a crystallographic hexamer (PDB ID code: 3Q9P, cyan). *Inset* shows the region around the β5–β6+7 loop that is ordered in our structure by a longer β6+7 β-strand that forms part of the dimer interface. (*C*) The longer N terminus in our construct allows formation of the β2 strand. (*D*) Differences in the β3–β4 loop between our structure and 3Q9P. (*E*) Repacking in the β-sandwich in cHSP27 compared with cABC. In aligning cABC to cHSP27, we find that F75 is replaced by the bulkier W95, L70 by H90, which disrupts van der Waals interactions in the core, and R149 by M169, which abolishes salt-bridges to both sides of the β-sandwich (specifically to D127 and carbonyl of E71).

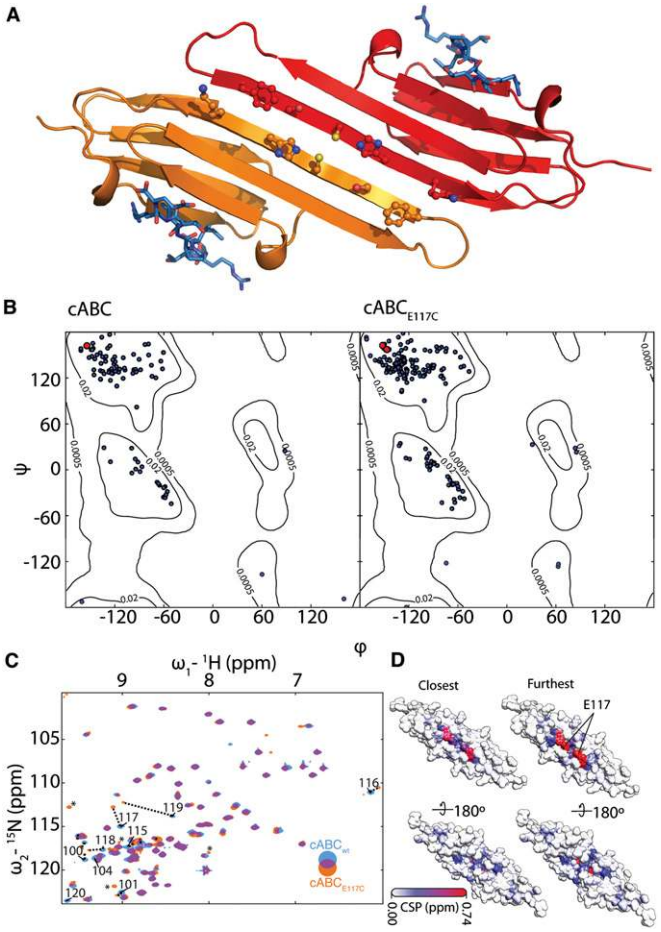

Fig. S2. (*A*) Second dimer in the asymmetric unit of the core domain of ABC (cABC$_{E117C}$), with the disulfide bond absent, likely as a consequence of radiation damage during data collection (1). The loop between β5 and β6+7 is ordered in this dimer. (*B*) C117 is not strained in cABC$_{E117C}$. Ramachandran plots for cABC (*Left*) and cABC$_{E117C}$ (*Right*). Red dots correspond to residue 117, which has normal β-sheet φ and ψ angles. Numbers on contour lines correspond to probabilities. The χ1 (65.37), χ2 (−33.22), χ3 (70.76), χ2′ (−44.41), and χ1′ (58.45) dihedral angles along the disulfide bond are within the range of unstrained cysteines. (*C*) A small number of resonances were difficult to assign in cABC$_{E117C}$ because several peaks in cABC$_{E117C}$ plausibly map to a peak in cABC. To deal with this ambiguity, two putative assignment lists for cABC$_{E117C}$ were produced. The first assumes that the resonance position in cABC$_{E117C}$ is furthest from that in cABC, and the second assumes that the resonance position in cABC$_{E117C}$ is closest to that in the cABC. The chemical-shift perturbation (CSP) values obtained in both cases are essentially identical. In the text, we show the assignment list assuming cABC$_{E117C}$ is furthest from cABC. Here, we show the assignment list assuming cABC$_{E117C}$ is nearest wild type. (*D*) The CSP values when mapped onto the structure of cABC are essentially indistinguishable.

1. Petrova T, et al. (2010) X-ray-induced deterioration of disulfide bridges at atomic resolution. *Acta Crystallogr D Biol Crystallogr* 66(Pt 10):1075–1091.

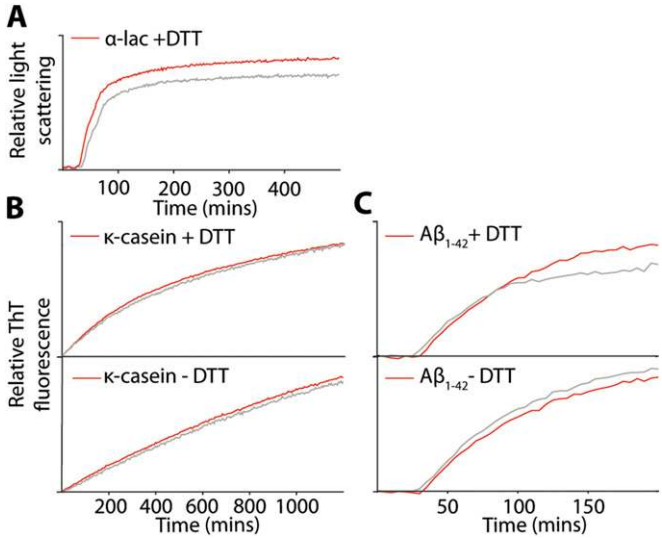

Fig. S3. Chaperone activity of cHSP27, equivalent to data presented for the ABC constructs in Fig. 5. Aggregation traces without chaperone are shown in red, and those with chaperone are shown in gray. cHSP27 is ineffective in protecting against the aggregation of (*A*) α-lactalbumin (α-lac), (*B*) κ-casein, and (*C*) $A\beta_{1–42}$. Molar ratios are the same as in the cABC experiments (main text).

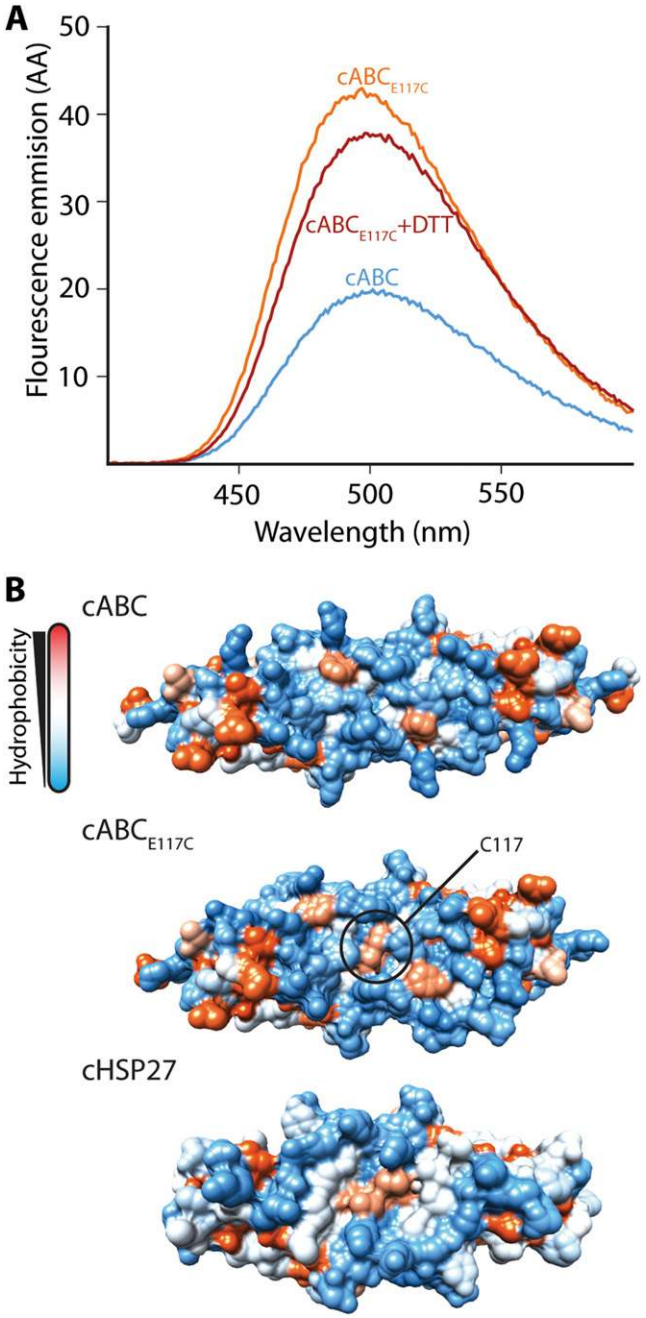

Fig. S4. Mutating E117 in cABC to a cysteine increases the exposed hydrophobic surface area of cABC$_{E117C}$. (*A*) bis-ANS (4,4′-dianilino-1,1′-binaphthyl-5,5′-disulfonic acid) binding to core domain forms of ABC reveals that cABC$_{E117C}$ displays higher bis-ANS fluorescence than cABC under both oxidizing and reducing conditions, suggesting an increased exposed hydrophobic surface in cABC$_{E117C}$. (*B*) Molecular surface of cABC, cABC$_{E117C}$, and cHSP27 colored according to Kyte–Doolittle hydrophobicity (1).

1. Kyte J, Doolittle RF (1982) A simple method for displaying the hydropathic character of a protein. *J Mol Biol* 157(1):105–132.

Table S1. Statistics of X-ray data collection and refinement for cABC, $cABC_{E117C}$, and cHSP27

	cABC	$cABC_{E117C}$	cHSP27
Crystal parameters			
Space group	I222	C2	$P2_1$
Cell dimensions			
a, b, c, Å	35.38, 47.86, 122.84	117.01, 46.77, 77.71	31.28, 48.96, 57.54
α, β, γ, degrees	90, 90, 90	90, 90, 90	90, 99.95, 90
Molecules in A.U.	2	8	4
Data collection			
Synchrotron beamline	APS (24-ID-C)	APS (24-ID-E)	In-house* (DSE-1.2)
Wavelength, Å	0.979	0.979	1.542
Resolution, Å	19.6–1.37	69–2.0	37–2.6
Reflections observed/unique	167,150/21,884	87,187/25,505	38,626/5,331
Completeness, %	97.5 (96.0) [†]	97.6 (97.52)	99.0 (89.5)
$R_{mrgd\text{-}F}$, %	4.5 (54.6)	6.9 (43.4)	7.8 (53.7)
I/σI	25.13 (3.33)	14.10 (3.5)	17.21 (3.2)
Refinement			
Resolution, Å	19.57–1.37	68.8–2.0	37–2.6
R_{work}, %[§]	15.6 (17.4)	19.3 (25.3)	23.4 (27.7)
R_{free}, %[¶]	18.8 (23.9)	24.4 (31.9)	26.6 (34.9)
No. of non-H atoms			
Protein	823	2993	1,397
Nonprotein	79	117	1
Avg. B-factors	24.2	40.1	50.5
Rmsd			
Bond length, Å	0.016	0.008	0.012
Bond angle, degrees	1.64	1.24	0.995
Registration state[‖]	AP_{III}	AP_{II}	AP_{II}
PDB ID code	4M5S	4M5T	4MJH

A.U., asymmetric unit.

*Data were collected using an FRD rotating anode generator with R-AXIS HTC imaging plate detector.

[†]Values in parentheses correspond to the highest-resolution shell.

[‡]$R_{mrgd\text{-}F} = (\Sigma|AI(h,P) - AI(h,Q)|)/(0.5* \Sigma\ AI(h,P) + AI(h,Q))$ where $AI = (\sqrt{I}$ if $I \geq 0$ or $-\sqrt{I}$ if $I < 0)$ as described previously (1).

[§]$R_{work} = \Sigma \mid F_o - F_c \mid / \Sigma\ F_o$.

[¶]R_{free} calculated using 5% of the data.

[‖]Registration state nomenclature as delineated previously (2).

1. Kabsch W (1993) Automatic processing of rotation diffraction data from crystals of initially unknown symmetry and cell constants. *J Appl Cryst* 26(6):795–800.
2. Laganowsky A, et al. (2010) Crystal structures of truncated alphaA and alphaB crystallins reveal structural mechanisms of polydispersity important for eye lens function. *Protein Sci* 19(5): 1031–1043.